Exchange current density of reversible solid oxide cell electrodes

Fukumoto, Takuro

Endo, Naoki

Natsukoshi, Katsuya

Tachikawa, Yuya

他

出版情報：International Journal of Hydrogen Energy. 47 (37), pp.16626-16639, 2022-04. Elsevier
バージョン：

Available online at www.sciencedirect.com

ScienceDirect

journal homepage: www.elsevier.com/locate/he

Exchange current density of reversible solid oxide cell electrodes

Takuro Fukumoto [a], *Naoki Endo* [a], *Katsuya Natsukoshi* [a], *Yuya Tachikawa* [a,b,c,d], *George F. Harrington* [c,e], *Stephen M. Lyth* [b,g], *Junko Matsuda* [b], *Kazunari Sasaki* [a,b,c,d,f,g,*]

[a] *Department of Hydrogen Energy Systems, Faculty of Engineering, Kyushu University, Motooka 744, Nishi-ku, Fukuoka 819-0395, Japan*

[b] *International Research Center for Hydrogen Energy, Kyushu University, Motooka 744, Nishi-ku, Fukuoka 819-0395, Japan*

[c] *Next-Generation Fuel Cell Research Center (NEXT-FC), Kyushu University, Motooka 744, Nishi-ku, Fukuoka 819-0395, Japan*

[d] *Center of Coevolutionary Research for Sustainable Communities, Kyushu University, Motooka 744, Nishi-ku, Fukuoka 819-0395, Japan*

[e] *Department of Materials Science and Engineering, Massachusetts Institute of Technology, Cambridge, MA 02139, USA*

[f] *Platform of Inter/Transdisciplinary Energy Research (Q-PIT), Kyushu University, Motooka 744, Nishi-ku, Fukuoka 819-0395, Japan*

[g] *International Institute for Carbon-Neutral Energy Research (WPI-I2CNER), Kyushu University, Motooka 744, Nishi-ku, Fukuoka 819-0395, Japan*

HIGHLIGHTS

- Reversible solid oxide cells with different electrode materials were fabricated.
- Apparent exchange current densities and activation energies were quantified.
- Ceria was found to accelerate the electrochemical reactions in electrolysis mode.
- Surface adsorption sites on the electrodes were found to be largely vacant.

GRAPHICAL ABSTRACT

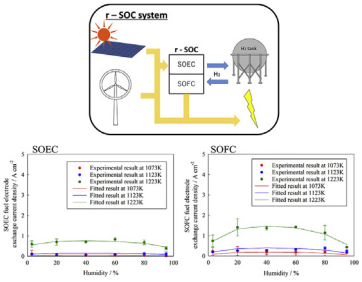

ARTICLE INFO

Article history:
Received 1 January 2022
Received in revised form

ABSTRACT

Reversible solid oxide cells (r-SOCs) can be operated in either solid oxide fuel cell or solid oxide electrolysis cell mode. They are expected to become important in the support of renewable energy due to their high efficiency for both power generation and hydrogen

* *Corresponding author*. Department of Hydrogen Energy Systems, Faculty of Engineering, Kyushu University, Motooka 744, Nishi-ku, Fukuoka 819-0395, Japan.
E-mail address: sasaki@mech.kyushu-u.ac.jp (K. Sasaki).

https://doi.org/10.1016/j.ijhydene.2022.03.164

16 March 2022
Accepted 17 March 2022
Available online 13 April 2022

generation. The exchange current density is one of the most important parameters in the quantification of electrode performance in solid oxide cells. In this study, four different fuel electrodes and two different air electrodes are fabricated using different materials and the microstructures are compared. The temperature, fuel humidification, and oxygen concentration at the air electrode are varied to obtain the apparent exchange current density for the different electrode materials. In contrast to ruthenium-and-gadolinia-doped ceria (Rh-GDC) as well as nickel-and-gadolinia-doped ceria (Ni-GDC) electrodes, significant differences in the apparent exchange current density were observed between electrolysis and fuel cell modes for the nickel-scandia-stabilized zirconia (Ni-ScSZ) cermet. Variation of gas concentration revealed that surface adsorption sites were almost completely vacant for all these electrodes. The apparent exchange current densities obtained in this study are useful as a parameter for simulation of the internal properties of r-SOCs.

Introduction

The introduction of renewable energy sources as an alternative to fossil fuels is crucial for the reduction of CO_2 emissions, and for the protection of the global environment. Sources of renewable energy such as solar and wind power exist in abundance on the earth, but one of the major obstacles in the expansion of their usage is intermittency [1–6]. Due to the fluctuation of power generation via renewable energy due to weather, time of day, and the season, energy storage systems should be developed which can play a role in matching supply and demand.

According to the Hydrogen Council report in 2017, hydrogen as a secondary energy carrier is expected to account for 18% of the world's energy demand in 2050, and about 20% of global carbon dioxide emission reductions by 2050 could be achieved through the widespread adoption of hydrogen technologies [7,8]. Hydrogen has the potential to: (i) enable large-scale integration of renewables for power generation; (ii) decentralize energy by sector and region; (iii) act as a buffer to increase system resilience; (iv) decarbonize transportation; (v) decarbonize industrial energy use; (vi) decarbonize heat and power in buildings; and (vii) provide a clean feedstock for industry [7]. These benefits are made possible by the fact that hydrogen is a clean energy carrier that emits only water when burned or converted to electricity. Therefore, hydrogen is expected to make a significant contribution to the realization of renewable energy systems with the ultimate goal of global decarbonization [7–12]. As the demand for hydrogen grows rapidly, water electrolysis technologies that can produce carbon-free green hydrogen from the electricity generated by renewable energy sources will be increasingly important.

Solid oxide electrolysis cells (SOECs) can produce hydrogen directly from steam using electrical energy. They are one of the most efficient methods for producing hydrogen gas, because they operate at high temperature [13–16], and incorporate a high degree of flexibility in design [13–16]. Solid oxide fuel cells (SOFCs) convert fuel to electricity, also with very high efficiency. A reversible solid oxide cell (r-SOC) combines the functions of both SOFCs and SOECs, depending on the situation [17–20]. They can supply electricity in SOFC mode when there is a shortage of power, or can produce hydrogen gas in SOEC mode when there is a surplus of power. In this way, r-SOCs can act as an energy storage device, compensating for the intermittency of renewable energies. From this viewpoint, r-SOCs are of significant technological interest.

Understanding the phenomena which occur inside r-SOCs is of great importance. However, it is challenging to experimentally visualize the spatial distribution of power generation and electrolysis-related phenomena inside the cell stacks due to the high operating temperature (around 800 °C). In previous work, we have performed visualization of the temperature distribution within SOFCs using a thermal imaging camera [21]. By comparing experimental results with numerical simulations of the cell geometry, we confirmed that internal phenomena such as gas distribution, current density distribution, and overvoltage distribution can be reliably simulated using the exchange current density as a parameter [21]. These results indicated that for numerical analysis, accurate measurement of the exchange current density is required to resolve issues related to the current density and temperature, such as thermal stress and high fuel utilization. The exchange current density describes electrochemical activity, and is indispensable in the simulation of electrode performance. We obtained an experimentally-derived concentration-dependent phenomenological equation for the exchange current density using a button cell with materials and structure matching those used in our simulations [21–26].

Simulations of SOFCs using the exchange current density as a parameter have been reported by e.g., Janardhanan et al., Dong et al. and Papurello et al. [22–26]. In contrast, there are few simulation studies focusing on the exchange current density in SOECs and r-SOCs [27,28]. However, systematic studies for multiple types of electrodes in SOECs and r-SOCs are lacking. In order to systematically compare the exchange current densities in SOFC and SOEC modes, these values must be measured using identical cells and common measurement protocols and procedures.

Here, the exchange current densities are obtained for model fuel and air electrodes using an r-SOC button cell. Four different fuel electrodes and two different air electrodes are investigated. The effects of systematically varying the humidification of the hydrogen fuel feed, the oxygen concentration of the air electrode supply gas, and the operating temperature are evaluated. The aim of this study is to clarify the effect of different operating conditions and electrode materials on the electrochemical performance of r-SOCs. Based on theoretical considerations made in a previous study by Hosoi et al. [29], the coverage of adsorption sites on SOFC/SOEC electrode surfaces during operation is considered.

The exchange current density represents the charge exchanged across the electrode/electrolyte interface under the open circuit conditions [30–32]. It is essentially an electrode-specific value, independent of the direction of the external current in either SOFC or SOEC mode. However, the exchange current density must be measured by passing a small current through the device, and therefore irreversible processes may affect the measured value. As such, the exchange current density obtained in this study is described more correctly as an "apparent exchange current density" obtained from experimental measurements.

Experimental

Cell preparation

Scandia-stabilized zirconia (ScSZ) plates (10 mol% Sc_2O_3 – 1 mol% CeO_2 – 89 mol% ZrO_2, Daiichi Kigenso Kagaku Kogyo Co., Ltd., Japan) with a diameter of 20 mm and a thickness of 200 μm were used as the solid oxide electrolyte. Two types of air electrodes were investigated in this study. The first, A-1, was a lanthanum strontium cobalt ferrite and gadolinium-doped ceria composite (LSCF/GDC), with a nominal composition of $(La_{0.6}Sr_{0.4})(Co_{0.2}Fe_{0.8})O_3/Gd_{0.1}Ce_{0.9}O_{2-\delta}$), sintered at 1100 °C for 2 h. The second, A-2, was lanthanum strontium manganate (LSM), with a nominal composition of $(La_{0.8}Sr_{0.2})_{0.98}MnO_3$, sintered at 1200 °C for 5 h. Meanwhile, four types of fuel electrode were investigated. The first, B-1, was a nickel-scandia-stabilized zirconia (Ni-ScSZ) cermet (in the form of NiO-ScSZ before reduction), sintered at 1300 °C for 3 h. The second, B-2, was ruthenium-and-gadolinia-doped ceria (Rh-GDC) co-impregnated on a lanthanum-doped strontium titanate and gadolinium-doped ceria (LST-GDC) composite with nominal composition $La_{0.1}Sr_{0.9}TiO_3$ and $Gd_{0.1}Ce_{0.9}O_2$, in the volume ratio of 50:50, and a ruthenium loading of 0.178 mg cm^{-2}, sintered at 1000 °C for 2 h. The third, B-3, was Ni-GDC co-impregnated on the same LST-GDC composite, with a nickel loading of 0.167 mg cm^{-2}, and sintered at 1000 °C for 2 h. The final fuel electrode, B-4, was a Ni-GDC cermet with a Ni:GDC volume ratio of 50:50, and sintered at 1300 °C for 3 h. Detailed preparation procedures of these co-impregnated fuel electrodes has been previously described by Futamura et al. [33]. The electrode area was 0.64 cm^2. It should be noted that apart from the chemical composition of the electrode materials, the porous microstructure (depending on factors such as sintering conditions) also affects electrode impedance and thus exchange current density.

Electrochemical evaluation

Automatic SOFC testing systems (Auto-SOFC, TOYO Co., Japan) were used for gas supply. The exchange current density i_0 was derived from the overvoltage values measured under SOFC and SOEC conditions using a Butler-Volmer type equation [29,34–36]. Apparent exchange current densities and activation energies were obtained by measuring the electrode impedance (Solartron Analytical, 1255WB, UK) at various current densities, and substituting the obtained overvoltage, absolute temperature, and current density values into the following Butler-Volmer-type equation (Eq. (1)):

$$i = i_0\left\{\exp\left(\frac{\overleftarrow{\alpha} nF\eta}{RT}\right) - \exp\left(-\frac{\overrightarrow{\alpha} nF\eta}{RT}\right)\right\} \quad (1)$$

where $\overleftarrow{\alpha}$ and $\overrightarrow{\alpha}$ are transfer coefficients ($\overleftarrow{\alpha} = \overrightarrow{\alpha} = 0.5$ [36–39]), n is the number of mobile electrons ($n = 2$ for fuel electrodes and $n = 4$ for air electrodes), F is Faraday's constant, R is the gas constant, T is the absolute temperature, i is the current density, and η is the activation (i.e. non-ohmic) overvoltage. The obtained exchange current densities were directly fitted with this generally used phenomenological equation for exchange current density. The exchange current densities of the electrodes and their dependence on various gas concentrations are compared and discussed.

The activation overvoltage was obtained by measuring the non-ohmic resistance R_{act} via impedance spectroscopy measurements, as shown in Fig. 1, and the following equation:

$$\eta = i \times R_{act} \quad (2)$$

This equation is based on the assumption that the concentration overvoltage is negligible in the low current density range (i = 0.05, 0.10, 0.15 A cm^{-2}) in solid oxide cells [40,41]. The obtained apparent exchange current densities at the air and fuel electrodes were plotted as a function of oxygen concentration at the air electrode and water vapor

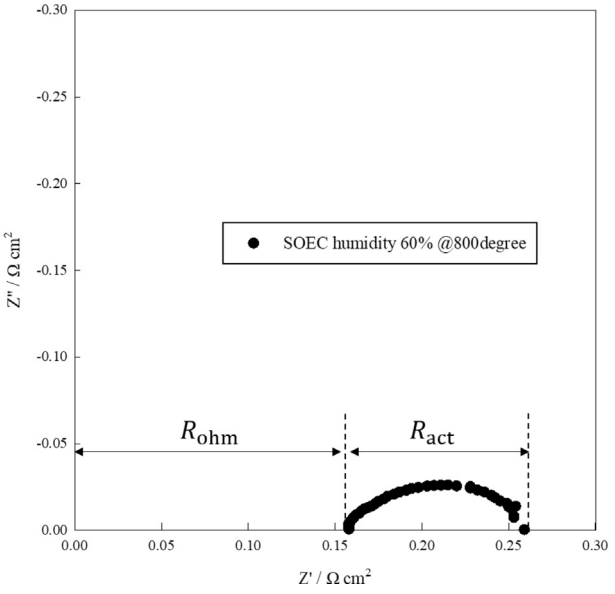

Fig. 1 – - Typical impedance spectrum of an SOEC operated with 60%-humidified H_2 at 800 °C.

concentration at the fuel electrode, respectively. The obtained exchange current densities are fitted with the following phenomenological equations [21,29,38,42–44], respectively.

Phenomenological equation for exchange current density of air electrodes:

$$i_{0,air} = \gamma_{air}\left(\frac{p_{O2}}{p_{O2,ref}}\right)^{A}\exp\left(-\frac{E_{a,air}}{RT}\right) \quad (3)$$

Phenomenological equation for exchange current density of fuel electrodes:

$$i_{0,fuel} = \gamma_{fuel}\left(\frac{p_{H2}}{p_{H2,ref}}\right)^{B}\left(\frac{p_{H2O}}{p_{H2O,ref}}\right)^{C}\exp\left(-\frac{E_{a,fuel}}{RT}\right) \quad (4)$$

here, $p_{H2,ref}$, $p_{H2O,ref}$, and $p_{O2,ref}$ are molar fractions of H_2, H_2O and O_2 gas, respectively. $p_{H2,ref}$, $p_{H2O,ref}$, and $p_{O2,ref}$ are set to be 97%, 3%, and 21%, respectively. γ_{fuel} and γ_{air} are the reaction rate constants for the fuel and air electrodes, A, B, and C are the various gas concentration dependent exponents, and $E_{a,fuel}$ and $E_{a,air}$ are the activation energies for the fuel and air electrode reactions, respectively.

Results and discussion

Apparent exchange current density at the air electrodes

The exchange current density is defined at the point where the electrode redox reactions are at equilibrium, therefore average values were obtained in the relatively low current density regions at i = 0.05, 0.10, and 0.15 A cm^{-2}, and plotted with error bars showing their standard deviation. Fig. 2 shows the dependence of the apparent exchange current density on the oxygen concentration in N_2+O_2 gas at the air electrodes, fitted using Eq. (3). The results show that the apparent exchange current density is higher for LSCF/GDC (A-1) than that for LSM (A-2) at the air electrode. This is attributed to the larger electrode reaction area, since LSM is well-known to be a pure electronic conductor, whereas LSCF is a mixed ionic electronic conductor (MIEC), resulting in electrode reactions occurring at both the three-phase boundaries and the two-phase boundaries [45–47]. The magnitudes of the apparent exchange current density were comparable for both SOFC and SOEC operation modes.

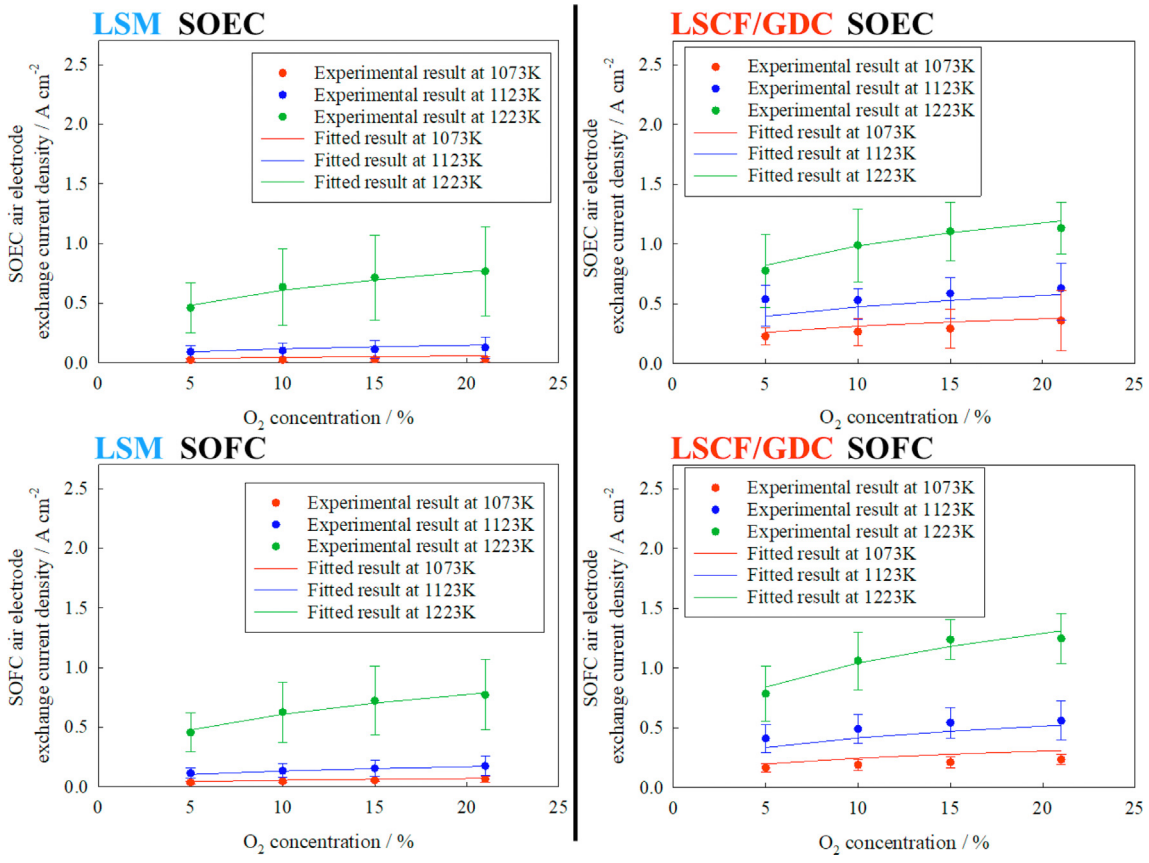

Fig. 2 – Apparent exchange current density of the air electrodes. (Fuel electrode: 3%-humidified hydrogen 100 mL min^{-1}; Air electrode: N_2 + O_2 150 mL min^{-1} (oxygen concentration: 5%, 10%, 15%, and 21%); Operating temperature: 800 °C, 850 °C, and 950 °C).

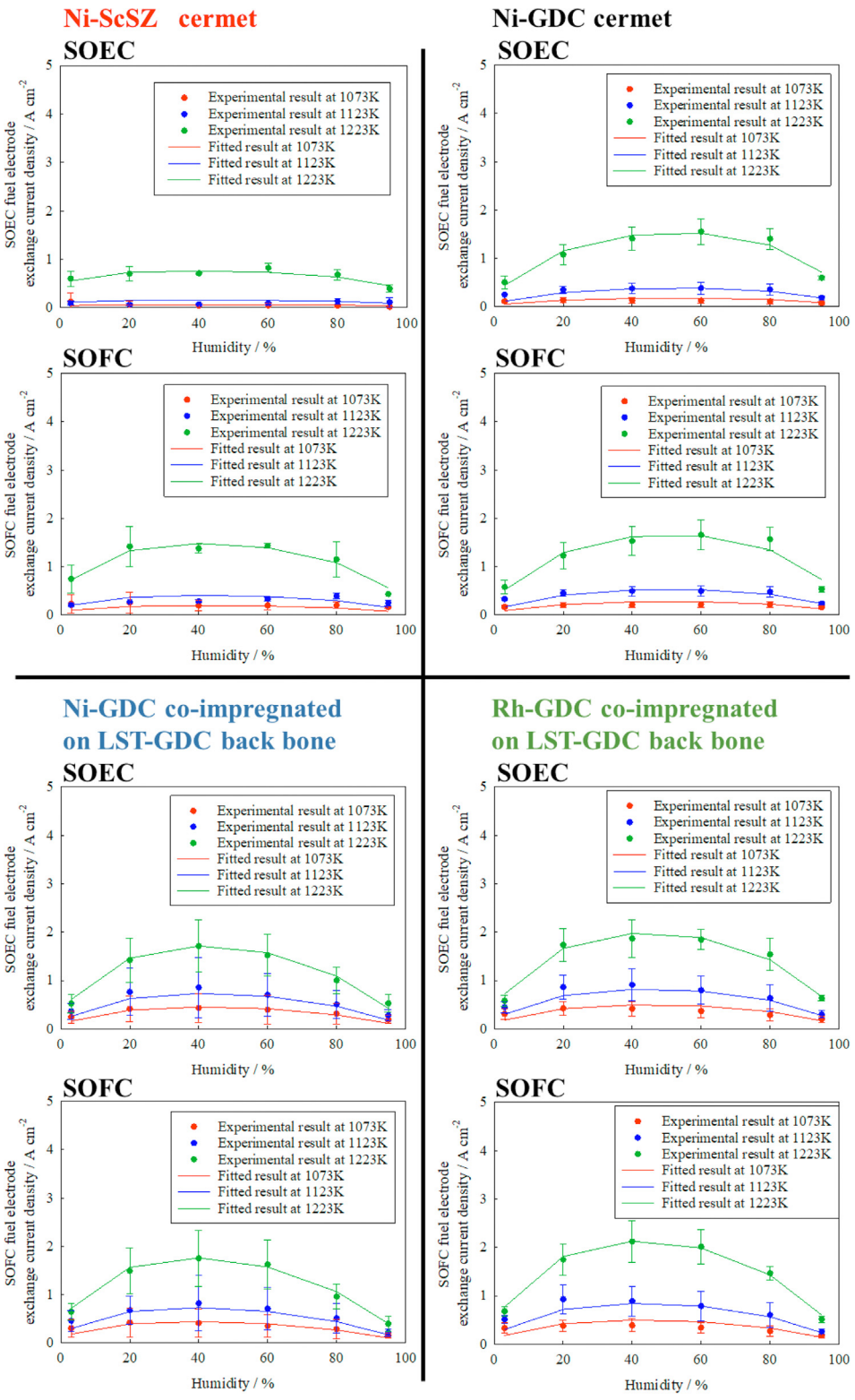

Fig. 3 – Apparent exchange current density of the fuel electrodes (Fuel electrode: $H_2 + H_2O$ 100 mL min^{-1} (humidity: 3%, 20%, 40%, 60%, 80%, and 95%); Air electrode: air 150 mL min^{-1}; Operating temperature: 800 °C, 850 °C, and 950 °C).

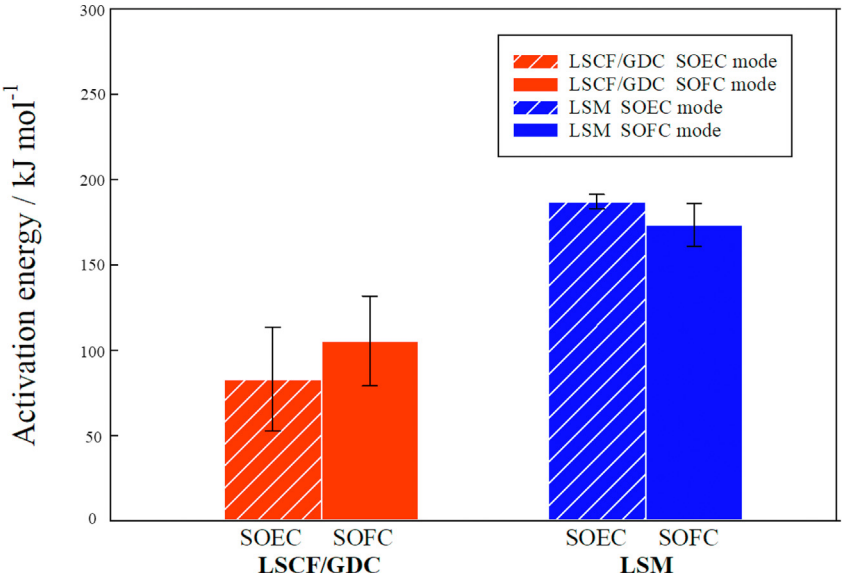

Fig. 4 – Activation energy of air electrode reactions derived using the phenomenological equation (Eq. (3)) for exchange current density of air electrodes, with error bars showing standard deviation.

Apparent exchange current density at the fuel electrodes

Fig. 3 shows the dependence of the apparent exchange current density on the water vapor concentration in the fuel (H_2+H_2O gas), at the fuel electrodes. These exchange current densities were obtained at i = 0.05, 0.10, and 0.15 A cm^{-2}, and the average values are plotted with error bars showing their standard deviation.

The apparent exchange current density was highest for B-2 (Rh-GDC co-impregnated on LST-GDC), and lowest for B-1 (the Ni-ScSZ cermet). This is attributed to the following points: (i) metallic Rh is more thermally and electrochemically stable than Ni and may have higher catalytic activity; (ii) the GDC surface itself acts as an electrode reaction site [48,49] due to the mixed ionic electronic conductivity of ceria under reducing conditions; and/or (iii) the two-dimensional cermet structure of Rh/Ni-GDC formed on the LST-GDC framework prevents aggregation of the catalyst particles [33].

Fig. 3 shows that the apparent exchange current density exhibits a maximum value at around 40–60% water vapor concentration for all the different fuel electrode materials, at a point where the concentration of reactants and products in the electrode reactions is comparable. The peaks in apparent exchange current density for the Ni-ScSZ cermet (B-1) and the Ni-GDC co-impregnated on LST-GDC (B-3) are slightly shifted to lower water vapor concentration compared to those of the Rh-GDC co-impregnated on LST-GDC (B-2) and the Ni-GDC cermet (B-1). This may be because Rh is more stable as a metal, and its catalytic activity can be maintained even in a highly-humidified atmosphere. In contrast, Ni can be more easily oxidized, resulting in a loss of catalytic activity at higher water vapor concentrations. The absence of this tendency in the Ni-GDC cermet could be caused by the catalytic activity of ceria for the oxygen exchange reaction associated with the valence change of ceria [48–50]. A higher proportion of GDC is used in the Ni-GDC cermet than in other Ni-based electrodes. Comparing SOFC and SOEC modes, the apparent exchange current density of the Ni-ScSZ cermet was higher in SOFC mode than in SOEC mode, whilst the values for the other three types of fuel electrode were similar. The apparent exchange current density of both the air and fuel electrodes increased with increasing temperature, which is consistent with the thermally activating nature of exchange current densities.

Table 1 – The apparent exchange current density in A cm^{-2} and the power of P_{O2} (A) at the air electrodes obtained in this study. Preexponential factors are given in A cm^{-2}, and activation energies are given in kJ mol^{-1}.

	SOEC		SOFC	
	Results fitted by Eq. (3)	A in Eq. (3)	Results fitted by Eq. (3)	A in Eq. (3)
LSM	$7.5\times10^{7}\cdot exp\left(-\frac{187}{RT}\right)\cdot\left(\frac{P_{O2}}{P_{O2,\,ref}}\right)^{0.33\pm0.03}$	0.33±0.03	$2.1\times10^{7}\cdot exp\left(-\frac{174}{RT}\right)\cdot\left(\frac{P_{O2}}{P_{O2,\,ref}}\right)^{0.35\pm0.06}$	0.35±0.06
LSCF/GDC	$4,200\cdot exp\left(-\frac{83}{RT}\right)\cdot\left(\frac{P_{O2}}{P_{O2,ref}}\right)^{0.26\pm0.09}$	0.26±0.09	$40,000\cdot exp\left(-\frac{105}{RT}\right)\cdot\left(\frac{P_{O2}}{P_{O2,ref}}\right)^{0.31\pm0.11}$	0.31±0.11

Comparison between SOFC and SOEC modes

At the different fuel electrodes, the exchange current density was found to be similar in both modes, or lower in SOEC mode compared to SOFC mode. One of the reasons for this may be that the electrode reaction is fundamentally different between SOFCs and SOECs. In SOFC mode, the major reactions at the fuel electrodes are dissociative reactions to break the H–H bonds of hydrogen gas molecules. Meanwhile in SOEC mode, the major reactions at the fuel electrodes are dissociative reactions to break the O–H bonds of water vapor molecules - the O–H bonds in H_2O have a higher molecular bond dissociation energy (118.8 kcal mol^{-1}) than the H–H bonds in H_2 (104.2 kcal mol^{-1}) [51]. This difference may explain the decrease in electrode reaction rate in SOEC mode.

The apparent exchange current density for the fuel electrodes increases by: (i) using Rh instead of Ni as a catalyst, and (ii) using GDC instead of ScSZ, promoting the electrode reactions. One of the reasons for the more pronounced difference in exchange current density between SOEC and SOFC modes for Ni-ScSZ compared to Rh-based and other Ni-based material electrodes could be due to catalytic activity. Rh is a noble metal and more redox-stable compared to Ni which is more easily oxidized, reducing the electrode activity, and leading to lower exchange current density. The ceria in LST-GDC is a mixed conductor that conducts both electrons and oxygen ions, and the Ce ions in ceria undergo a valence change between trivalent and tetravalent [48–50]. This valence change leads to flexible oxygen surface exchange reactions, increasing the catalytic activity. Both co-impregnated GDC and LST-GDC structures contain ceria, and may also therefore act as catalysts for the electrochemical reactions, especially in the case of steam electrolysis.

Activation energy of the air electrode reactions

In this study, we measured the dependence of the apparent exchange current density of both electrodes on temperature and various gas concentrations. The activation energies were also derived from the temperature dependencies using Eqs. (3) and (4). The activation energy of the exchange current density of the air electrode, derived using Eq. (3), is shown in Fig. 4.

The activation energy of the LSCF/GDC electrode (A-1) was clearly lower than that of the LSM electrode (A-2). This difference can be easily understood, as LSM is a pure electronic conductor while LSCF/GDC is mixed conducting electrode with extended electrode reaction sites, as mentioned before. A comparison between the SOFC and SOEC modes is of scientific interest. The mixed conducting LSCF/GDC electrode exhibits slightly lower activation energy in SOEC mode, compared to SOFC mode. In contrast, the activation energies measured in SOEC and SOFC modes are comparable for the LSM electrode where electrode reactions occur at the three-phase boundaries. These results suggest that mixed ionic electronic conductivity which expands the electrode reaction region promotes the fuel electrode reactions, especially in SOEC mode.

Fitted values of the apparent current density at the air electrodes obtained in this study are compiled in Table 1. Several reports on the activation energy of electrode reactions in SOFCs obtained from the exchange current density have already been published. As the activation energy for the air electrode reactions, Nagata et al. reported 130 kJ mol^{-1}, where LSM was used as the electrode and YSZ was used as the electrolyte [52], and Costamagna et al. reported 120 kJ mol^{-1} [25]. For SOECs, Udagawa et al. reported the activation energy of the air electrode reactions to be 137 kJ mol^{-1} [53]. For both SOFC and SOEC modes, the values are comparable to those obtained in this study, shown in Fig. 4 and compiled in Table 1.

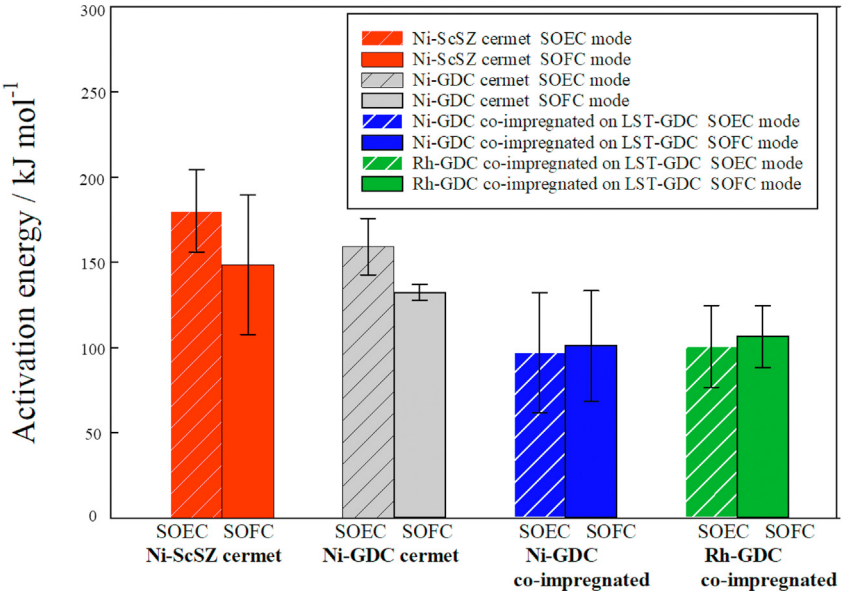

Fig. 5 – Activation energy of the fuel electrode reactions derived using the phenomenological equation (Eq. (4)) for exchange current density of fuel electrodes, with error bars showing standard deviation.

Table 2 – - The apparent exchange current density in A cm^{-2} and the power of P_{H2} (B) and P_{H2O} (C) of the fuel electrodes obtained in this study. Preexponential factors are given in A cm^{-2}, and activation energies are given in kJ mol^{-1}.

	SOEC		SOFC	
	Results fitted by Eq. (4)	B, C	Results fitted by Eq. (4)	B, C
Ni-ScSZ cermet	$2.7\times10^{7}\cdot exp\left(-\frac{180}{RT}\right)\cdot\left(\frac{P_{H2}}{P_{H2,ref}}\right)^{0.27\pm0.09}\cdot\left(\frac{P_{H2O}}{P_{H2O,ref}}\right)^{0.17\pm0.09}$	B = 0.27±0.01 C = 0.17±0.09	$1.7\times10^{6}\cdot exp\left(-\frac{149}{RT}\right)\cdot\left(\frac{P_{H2}}{P_{H2,ref}}\right)^{0.52\pm0.04}\cdot\left(\frac{P_{H2O}}{P_{H2O,ref}}\right)^{0.37\pm0.11}$	B = 0.52±0.04 C = 0.37±0.11
Ni-GDC cermet	$2.7\times10^{6}\cdot exp\left(-\frac{159}{RT}\right)\cdot\left(\frac{P_{H2}}{P_{H2,ref}}\right)^{0.49\pm0.02}\cdot\left(\frac{P_{H2O}}{P_{H2O,ref}}\right)^{0.56\pm0.02}$	B = 0.49±0.02 C = 0.56±0.02	$2.2\times10^{5}\cdot exp\left(-\frac{132}{RT}\right)\cdot\left(\frac{P_{H2}}{P_{H2,ref}}\right)^{0.51\pm0.03}\cdot\left(\frac{P_{H2O}}{P_{H2O,ref}}\right)^{0.54\pm0.05}$	B = 0.51±0.03 C = 0.54±0.05
Ni-GDC co-impregnated on LST-GDC	$8,400\cdot exp\left(-\frac{97}{RT}\right)\cdot\left(\frac{P_{H2}}{P_{H2,ref}}\right)^{0.75\pm0.06}\cdot\left(\frac{P_{H2O}}{P_{H2O,ref}}\right)^{0.54\pm0.07}$	B = 0.75±0.06 C = 0.54±0.07	$14,700\cdot exp\left(-\frac{101}{RT}\right)\cdot\left(\frac{P_{H2}}{P_{H2,ref}}\right)^{0.77\pm0.14}\cdot\left(\frac{P_{H2O}}{P_{H2O,ref}}\right)^{0.49\pm0.06}$	B = 0.77±0.14 C = 0.49±0.06
Rh-GDC co-impregnated on LST-GDC	$14,900\cdot exp\left(-\frac{101}{RT}\right)\cdot\left(\frac{P_{H2}}{P_{H2,ref}}\right)^{0.61\pm0.11}\cdot\left(\frac{P_{H2O}}{P_{H2O,ref}}\right)^{0.50\pm0.06}$	B = 0.61±0.11 C = 0.50±0.06	$26,000\cdot exp\left(-\frac{106}{RT}\right)\cdot\left(\frac{P_{H2}}{P_{H2,ref}}\right)^{0.69\pm0.08}\cdot\left(\frac{P_{H2O}}{P_{H2O,ref}}\right)^{0.52\pm0.03}$	B = 0.69±0.08 C = 0.52±0.03

Activation energy of the fuel electrode reactions

Fig. 5 shows the activation energy obtained from the temperature dependence of the exchange current density for the four different materials used for the fuel electrode in both SOFC and SOEC modes.

The activation energy was highest for the Ni-ScSZ cermet electrode (B-1). When the electrolyte component in the cermet electrodes was changed from ScSZ to GDC, the activation energy slightly decreased. When the electrode was changed from the cermet electrodes to a co-impregnated fuel electrode with GDC, the activation energy further decreased. The co-impregnated electrodes with Ni and Rh catalysts exhibit similar activation energy. These tendencies imply that replacing ScSZ (a pure ionic conductor), with GDC (a mixed ionic and electronic conductor) promotes the electrode reactions. Furthermore, the electrode reactions were further accelerated by tailoring the impregnated two-dimensional cermet structure with the GDC mixed conductor [33]. Mixed conductivity and tailored microstructure can decrease the activation energy of the exchange current density, for the design of high-performance fuel electrodes.

The activation energies in SOFC and SOEC modes were also compared, and the results were identical within error. However, the activation energy obtained in SOEC mode tended to increase for both Ni-ScSZ and Ni-GDC cermet fuel electrodes. As previously mentioned, in SOFC mode, the fuel electrode breaks H–H bonds, while in SOEC mode, the fuel electrode breaks O–H bonds, leading to an increase in activation energy for SOEC mode. In contrast, there was no significant difference in the activation energy between SOFC and SOEC modes for the co-impregnated fuel electrodes, but the activation energy in SOEC mode seems to be slightly lower. Further studies are of scientific and technological relevance to understand these differences and to further reduce the activation energy by varying the ratio of Ni/Rh and GDC, and by optimizing electrode microstructure.

Fitted values of the apparent exchange current density at the fuel electrodes obtained in this study are compiled in Table 2. As the activation energy for the fuel electrode reactions of SOFC, Nagata et al. reported 120 kJ mol^{-1} [52], where Ni-YSZ was used as the electrode and YSZ was used as the electrolyte. Costamagna et al. reported 100 kJ mol^{-1} [25]. In SOEC mode, Udagawa et al. reported the activation energy of the fuel electrode reaction to be 140 kJ mol^{-1} [53]. In both SOFC and SOEC modes, the values are comparable to those obtained in this study, shown in Fig. 5 and compiled in Table 2.

On possible elementary processes

Possible elementary processes occurring at the SOFC/SOEC electrodes can be further discussed, following previous discussions by Hosoi et al. [29]. Possible electrode reactions at the

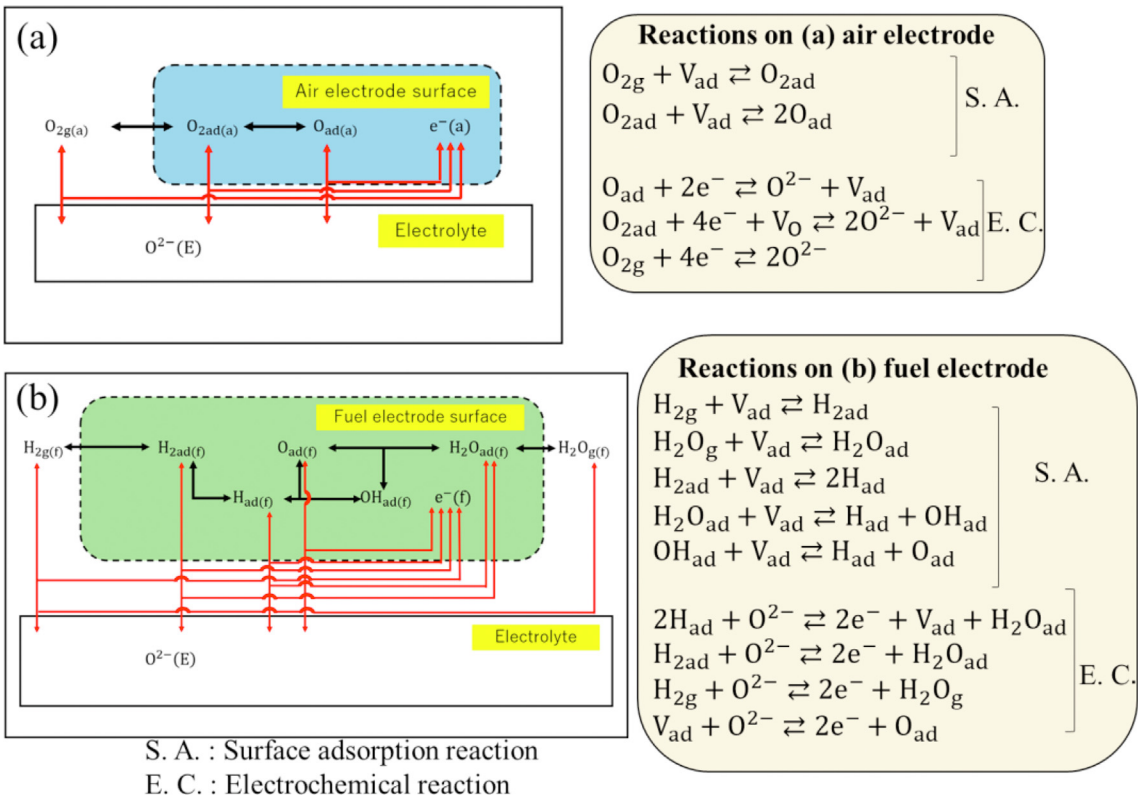

Fig. 6 – Possible reactions on (a) the air electrode and (b) the fuel electrode, after Hosoi et al. [29]. The subscript "ad" denotes an adsorbed species or an adsorption site. The subscript "g" denotes a gas molecule.

air and fuel electrodes may be considered as described in Fig. 6(a) and (b), respectively. Assuming rate-determining reactions, the relationship between the various gas concentration-dependent indices A, B, and C in the general phenomenological equations (Eqs. (3) and (4)) and coverage of the adsorption sites on the electrode surface have both been derived [29]. These values were compared with those obtained experimentally in this study.

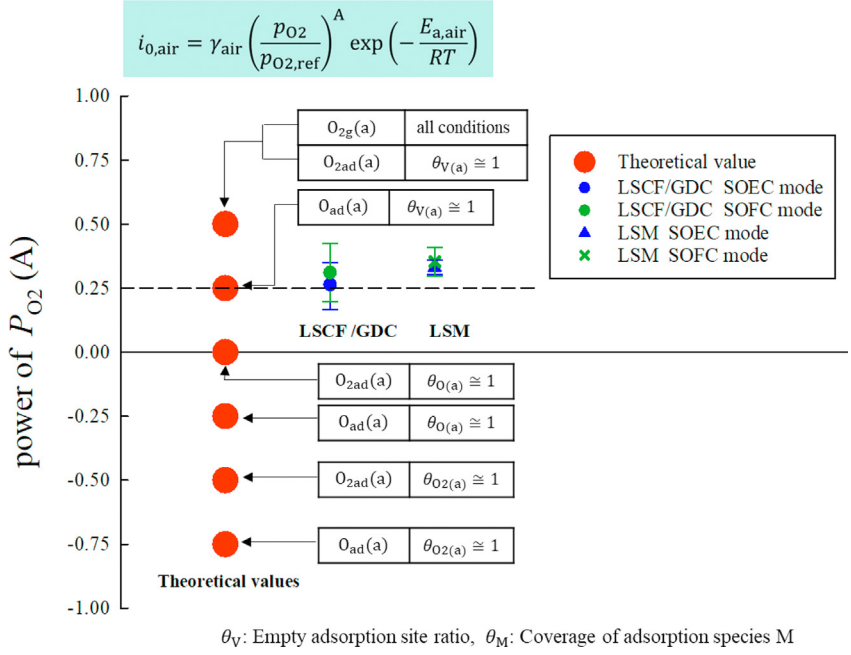

Fig. 7 – Air electrode surface coverage ($\theta_{(a)}$) and gas concentration dependence, analyzed using the p_{O2} dependencies compiled by Hosoi et al. [29].

Table 3 – – Electrochemical reactions assumed as rate-determining reactions [29] in Figs. 7 and 8.

	Reactive species shown on the left side in the text boxes in Figs. 7 and 8	Rate-determining reactions assumed
Air electrode	$O_{ad}(a)$	$O_{ad} + 2e^- \rightleftarrows O^{2-} + V_{ad}$
	$O_{2ad}(a)$	$O_{2ad} + 4e^- + V_O \rightleftarrows 2O^{2-} + V_{ad}$
	$O_{2g}(a)$	$O_{2g} + 4e^- \rightleftarrows 2O^{2-}$
Fuel electrode	$H_{ad}(f)$	$2H_{ad} + O^{2-} \rightleftarrows 2e^- + V_{ad} + H_2O_{ad}$
	$H_{2ad}(f)$	$H_{2ad} + O^{2-} \rightleftarrows 2e^- + H_2O_{ad}$
	$H_{2g}(f)$	$H_{2g} + O^{2-} \rightleftarrows 2e^- + H_2O_g$
	$V_{ad}(f)$	$V_{ad} + O^{2-} \rightleftarrows 2e^- + O_{ad}$

Fig. 7 and Table 1 show the relationship between the oxygen concentration-dependent index A in the phenomenological equation of the exchange current density of the air electrode and the coverage of the adsorption sites on the air electrode surface. Table 3 shows the species shown on the left side in the text boxes in Figs. 7 and 8 and the rate-determining reactions. The values of A were close to 0.25 in both SOEC and SOFC modes for both LSCF/GDC and LSM. The theoretical discussion by Hosoi et al. [29] described in Fig. 7 suggests that the surface coverages of these air electrodes (LSCF/GDC and LSM) are $\theta_V \cong 1 \gg \theta_O$, θ_{O2}, which means that the electrode surface adsorption sites are almost empty. It is understandable that the coverage is close to zero, due to the high operating temperature of SOFCs and SOECs, leading to higher thermal mobility of adsorbed species. In the LSM, the plots shift upward and approach the point where A = 0.5. This suggests that the rate-determining reaction could include not only O_{ad} (A = 0.25), but also O_{2ad} and O_{2g} (A = 0.5) [29].

In Fig. 8, the relationship between the hydrogen concentration-dependent index B (y-axis) and the water vapor concentration-dependent index C (x-axis), and the coverage of adsorption sites on the fuel electrode surface for Ni-ScSZ, Ni-GDC, and Rh-GDC fuel electrodes is also considered and described. The values of B and C are close to 0.5 in both SOFC

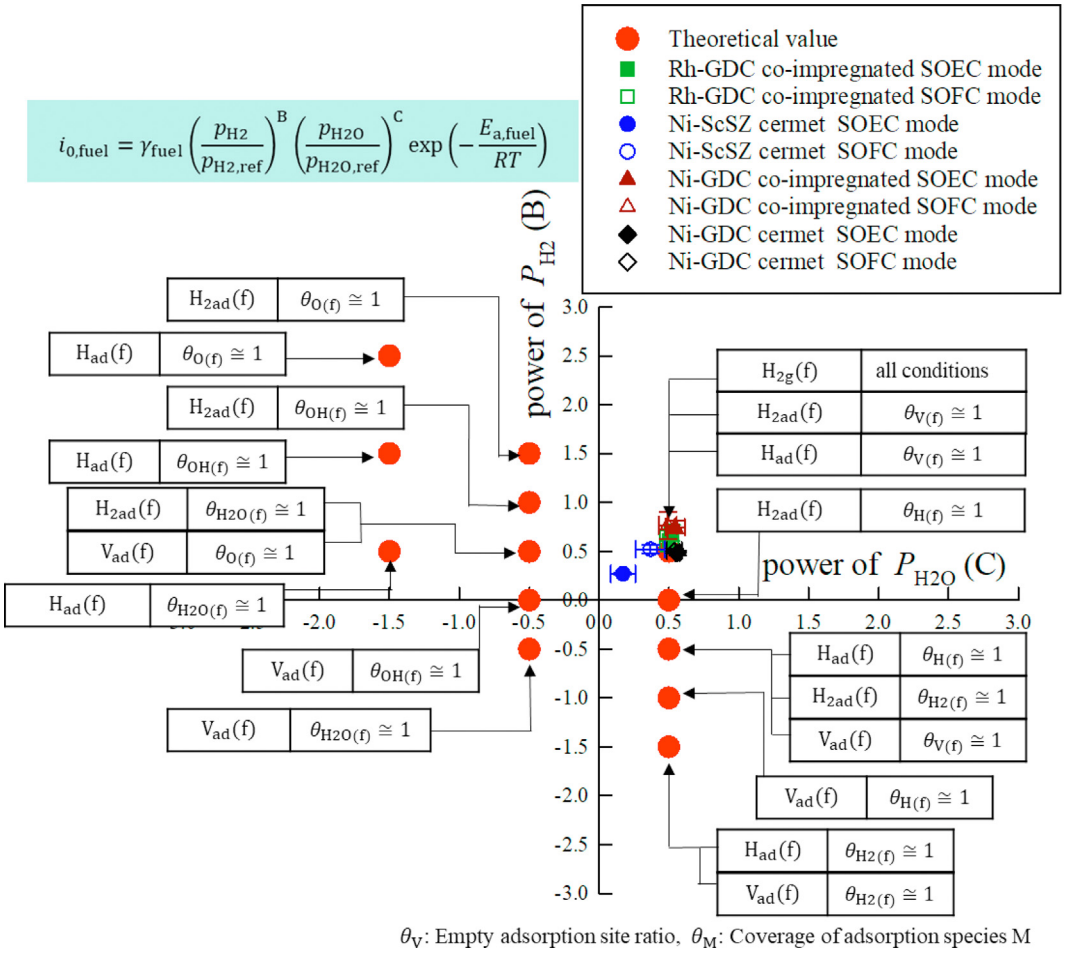

Fig. 8 – Fuel electrode surface coverage ($\theta_{(f)}$) and gas concentration dependence, analyzed using the p_{H2} and p_{H2} dependencies compiled by Hosoi et al. [29].

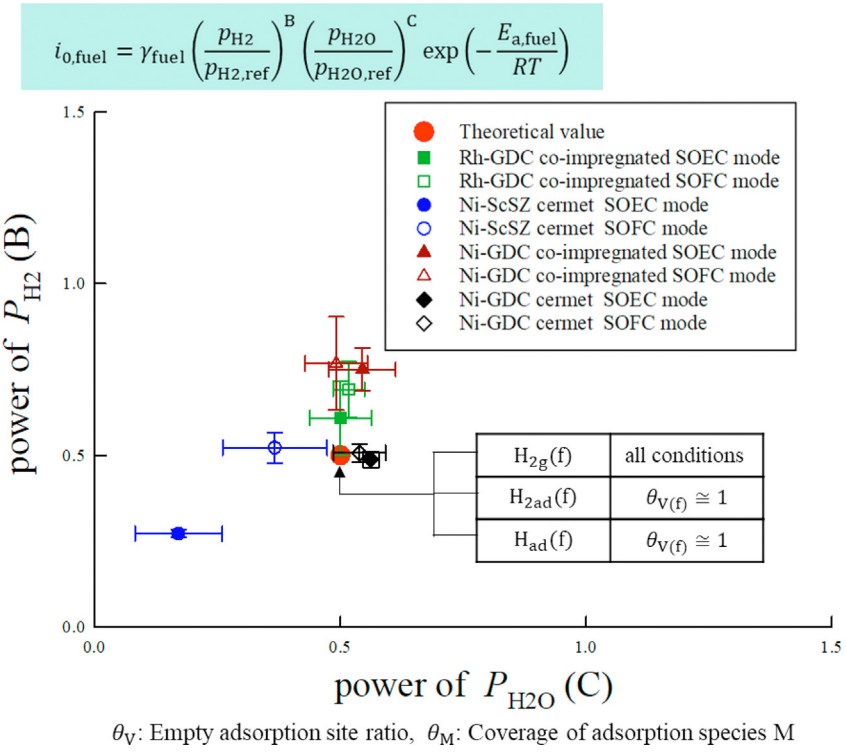

Fig. 9 – Fuel electrode surface coverage and gas concentration dependence.

and SOEC modes. The relation $\theta_V \cong 1 \gg \theta_H, \theta_{H2O}, \theta_{OH}, \theta_O$ means that the electrode surface adsorption sites are again almost empty. Similar to the air electrode surface, the thermal mobility of surface species is high at high temperatures, leading to low coverage on the fuel electrodes at normal SOFC/SOEC operating temperatures.

Fig. 9 summarizes the exponents of the gas species concentration dependence obtained experimentally at the fuel electrodes in this study. As shown in this figure, the values of B and C are close to 0.5. Exactly speaking, the values of B and C are closer to 0.5 for the Rh-GDC co-impregnated on LST-GDC and Ni-GDC cermet than for the Ni-ScSZ cermet and the Ni-GDC co-impregnated on LST-GDC. This can be explained by the fact that Rh is stable as a metal so that the adsorption sites tend to be completely empty. Another possible factor is the influence of mixed conducting GDC with high surface exchange reaction activity. Such catalytic activity of GDC in GDC-containing fuel electrodes maintains sufficient adsorption sites for both SOFC and SOEC electrode reactions.

For the Ni-ScSZ cermet electrode, the plot in the figure shifts to the lower left in the SOEC mode, approaching the point where B = C = −0.5 in Fig. 8, suggesting that the electrode surface may be partially covered with H2O under high water vapor atmosphere, accounting for the low activity in SOEC mode.

Conclusions

Electrodes for r-SOCs were prepared with different constituent materials and structures, and were systematically evaluated to quantify the exchange current density in both SOFC and SOEC modes. Similar gas concentration dependence was obtained for both fuel and air electrodes in both SOFC and SOEC modes, and it was deduced that the surface adsorption sites of both electrodes were almost empty. The apparent exchange current densities and their activation energy quantitatively indicate the difference in reaction processes between SOFC and SOEC modes, and a high electrocatalytic activity of mixed conducting GDCs, especially in SOEC mode.

In this study, hydrogen was used as the fuel. However, r-SOCs can also supply various fuels other than hydrogen and this should be considered in future studies. In addition, inactivation of the fuel electrode by trace pollutants [54–57] in e.g. biofuel streams should also be considered.

Declaration of competing interest

The authors declare that they have no known competing financial interests or personal relationships that could have appeared to influence the work reported in this paper.

Acknowledgments

A part of this study was supported by "Research and Development Program for Promoting Innovative Clean Energy Technologies Through International Collaboration" of the New Energy and Industrial Technology Development Organization (NEDO) (Contract No. 20001460-0). Collaborative support by Prof. H. L. Tuller, Prof. B. Yildiz, and Prof. J. L. M. Rupp at

Massachusetts Institute of Technology (MIT) is gratefully acknowledged.

Nomenclature

Notation description unit

A	Oxygen concentration dependent exponents for phenomenological equation for exchange current density of air electrodes
B	Hydrogen concentration dependent exponents for phenomenological equation for exchange current density of fuel electrodes
C	Water vapor concentration dependent exponents for phenomenological equation for exchange current density of fuel electrodes
e^-	electron
E_a	the activation energy kJ/mol
F	Faraday's constant, 96,485 C mol^{-1}
i	current density A cm^{-2}
i_0	exchange current density A cm^{-2}
n	the number of mobile electrons
M	species M (M = H, H_2, H_2O, O, and O_2)
p_M	concentration of gas M (molar fraction) %
R	the gas constant, 8.3145 J mol^{-1} K^{-1}
R_{act}	the non-ohmic resistance Ω cm^2
T	the absolute temperature K
V_{ad}	empty adsorption sites of the electrode
V_O	oxygen vacancies in the electrolyte

Greek symbols

$\overleftarrow{\alpha}, \overrightarrow{\alpha}$	transfer coefficients
γ	preexponential factors for exchange current density equations A cm^{-2}
η	the activation (non-ohmic) overvoltage V
θ_M	coverage of M on the adsorption site of the electrode
θ_V	empty adsorption site ratio of the electrode

Abbreviations, subscripts and superscripts

(a)	the species on the air electrode
ad	the species adsorbed on the adsorption site of the electrode
air	the parameters for the air electrode
(E)	subscript attached to the species in the electrolyte
(f)	the species on the fuel electrode
fuel	the parameters for the fuel electrode
g	gaseous state
GDC	gadolinia-doped ceria
LSCF	lanthanum strontium cobalt ferrite
LSM	lanthanum strontium manganite
LST	lanthanum strontium titanate
Ni	nickel
ref	reference
Rh	rhodium
r-SOC	reversible solid oxide cell
ScSZ	scandia-stabilized zirconia
SOFC	solid oxide fuel cell
SOEC	solid oxide electrolysis cell
YSZ	yttria-stabilized zirconia

REFERENCES

[1] Akinyele DO, Rayudu RK. Review of energy storage technologies for sustainable power networks. Sustain Energy Technol Assessments 2014;8:74–91. https://doi.org/10.1016/j.seta.2014.07.004.

[2] Pellow MA, Emmott CJM, Barnhart CJ, Benson SM. Hydrogen or batteries for grid storage? A net energy analysis. Energy Environ Sci 2015;8:1938–52. https://doi.org/10.1039/C4EE04041D.

[3] Feng Q, Yuan XZ, Liu G, Wei B, Zhang Z, Li H, Wang H. A review of proton exchange membrane water electrolysis on degradation mechanisms and mitigation strategies. J Power Sources 2017;366:33–55. https://doi.org/10.1016/j.jpowsour.2017.09.006.

[4] Ni MN, Leung MKH, Leung DYC. Technological development of hydrogen production by solid oxide electrolyzer cell (SOEC). Int J Hydrogen Energy 2008;33:2337–54. https://doi.org/10.1016/j.ijhydene.2008.02.048.

[5] Luo Y, Shi Y, Zheng Y, Cai N. Reversible solid oxide fuel cell for natural gas/renewable hybrid power generation systems. J Power Sources 2017;340:60–70. https://doi.org/10.1016/j.jpowsour.2016.11.057.

[6] Schmidt O, Gambhir A, Staffell I, Hawkes A, Nelson J, Few S. Future cost and performance of water electrolysis: an expert elicitation study. Int J Hydrogen Energy 2017;42:30470–92. https://doi.org/10.1016/j.ijhydene.2017.10.045.

[7] Hydrogen Council. Scaling up. November 2017. https://hydrogencouncil.com/wp-content/uploads/2017/11/Hydrogen-scaling-up-Hydrogen-Council.pdf.

[8] International Energy Agency. The future of hydrogen. 2019. https://www.iea.org/hydrogen2019/.

[9] Mazloomi K, Gomes C. Hydrogen as an energy carrier: prospects and challenges. Renew Sustain Energy Rev 2012;16:3024–33. https://doi.org/10.1016/j.rser.2012.02.028.

[10] Momirlan M, Veziroglu TN. The properties of hydrogen as fuel tomorrow in sustainable energy system for a cleaner planet. Int J Hydrogen Energy 2005;30:759–802. https://doi.org/10.1016/j.ijhydene.2004.10.011.

[11] Møller KT, Jensen TR, Akiba E, Li H. Hydrogen - a sustainable energy carrier. Prog Nat Sci: Mater Int 2017;27:34–40. https://doi.org/10.1016/j.pnsc.2016.12.014.

[12] Ley MB, Jepsen LH, Lee Y, Cho YW, Colbe JMB, Dornheim M, Rokin M, Jensen JO, Sloth M, Filinchuk Y, Jørgensen JE, Besenbacher F, Jensen TR. Complex hydrides for hydrogen storage - new perspectives. Mater Today 2014;17:122–8. https://doi.org/10.1016/j.mattod.2014.02.013.

[13] Jacobson AJ. Materials for solid oxide fuel cells. Chem Mater 2010;22:660–74. https://doi.org/10.1021/cm902640j.

[14] Singhal SC, Kendall K. High temperature solid oxide fuel cells. Elsevier; 2003, ISBN 978-0-080-50808-5.

[15] Matsuzaki Y, Tachikawa Y, Somekawa T, Hatae T, Matsumoto H, Taniguchi S, Sasaki K. Effect of proton-conduction in electrolyte on electric efficiency of multi-stage solid oxide fuel cells. Sci Rep 2015;5:12640–50. https://doi.org/10.1038/srep12640.

[16] Brett DJL, Atkinson A, Brandon NP, Skinner SJ. Intermediate temperature solid oxide fuel cells. Chem Soc Rev 2008;37:1568–78. https://doi.org/10.1039/b612060c.

[17] Minh NQ, Mogensen MB. Reversible solid oxide fuel cell technology for green fuel and power production. Interface 2013;22:55–62. https://doi.org/10.1149/2.F05134IF.

[18] Mogensen MB, Chen M, Frandsen HL, Graves C, Hansen JB, Hansen KV, Hauch A, Jacobsen T, Jensen SH, Skafte TL, Sun X. Reversible solid-oxide cells for clean and sustainable

energy. Clean Energy 2019;3:175–201. https://doi.org/10.1093/ce/zkz023.
[19] Natsukoshi K, Miyara K, Tachikawa Y, Matsuda J, Taniguchi S, Harrington GF, Sasaki K. Reversible solid oxide cells: durability of fuel electrodes against voltage cycling. ECS Trans 2021;103(1):375–82. https://doi.org/10.1149/10301.0375ecst.
[20] Shen M, Ai F, Ma H, Xu H, Zhang Y. Progress and prospects of reversible solid oxide fuel cell materials. iScience 2021;24:103464. https://doi.org/10.1016/j.isci.2021.103464.
[21] Takino K, Tachikawa Y, Mori K, Lyth SM, Shiratori Y, Taniguchi S, Sasaki K. Simulation of SOFC performance using a modified exchange current density for pre-reformed methane-based fuels. Int J Hydrogen Energy 2020;45:6912–25. https://doi.org/10.1016/j.ijhydene.2019.12.089.
[22] Janardhanan VM, Deutschmann O. Modeling of solid-oxide fuel cells. Z Phys Chem 2007;221:443–78. https://doi.org/10.1524/zpch.2007.221.4.443.
[23] Dong SK, Jung WN, Rashid K, Kashimoto A. Design and numerical analysis of a planar anode-supported SOFC stack. Renew Energy 2016;94:637–50. https://doi.org/10.1016/j.renene.2016.03.098.
[24] Xu M, Li TS, Yang M, Andersson M, Fransson I, Larsson T, Sunden B. Modeling of an anode supported solid oxide fuel cell focusing on thermal stresses. Int J Hydrogen Energy 2016;41:14927–40. https://doi.org/10.1016/j.ijhydene.2016.06.171.
[25] Costamagna P, Selimovic A, Borghi MD, Agnew G. Electrochemical model of the integrated planar solid oxide fuel cell (IP-SOFC). Chem Eng J 2004;102:61–9. https://doi.org/10.1016/j.cej.2004.02.005.
[26] Papurello D, Canuto D, Santarelli M. CFD model for tubular SOFC stack fed directly by biomass. Int J Hydrogen Energy 2022;47:6860–72. https://doi.org/10.1016/j.ijhydene.2021.12.015.
[27] Tao Y, Nishino H, Ashidate S, Kokubo H, Watanabe M, Uchida H. Polarization properties of La0.6Sr0.4Co0.2Fe0.8O3-based double layer-type oxygen electrodes for reversible SOFCs. Electrochim Acta 2009;54:3309–15. https://doi.org/10.1016/j.electacta.2008.12.048.
[28] Shimura K, Nishino H, Kakinuma K, Brito ME, Uchida H. Effect of samaria-doped ceria (SDC) interlayer on the performance of $La_{0.6}Sr_{0.4}Co_{0.2}Fe_{0.8}O_{3-\delta}$/SDC composite oxygen electrode for reversible solid oxide fuel cells. Electrochim Acta 2017;225:114–20. https://doi.org/10.1016/j.electacta.2016.12.100.
[29] Hosoi T, Yonekura T, Sunada K, Sasaki K. Exchange current density of SOFC electrodes: theoretical relations and partial pressure dependencies rate-determined by electrochemical reactions. J Electrochem Soc 2015;162:F136–52. https://doi.org/10.1149/2.0561501jes.
[30] Liu Y, Xu X, Sadd M, Kapitanova OO, Krivchenko VA, Ban J, Wang J, Jiao X, Song Z, Song J. Insight into the critical role of exchange current density on electrodeposition behavior of lithium metal. Adv Sci 2021;8. https://doi.org/10.1002/advs.202003301. 2003301-12.
[31] Nørskov JK, Bligaard T, Logadottir A, Kitchin JR, Chen JG, Pandelov S, Stimming U. Trends in the exchange current for hydrogen evolution. J Electrochem Soc 2005;152:J23–6. https://doi.org/10.1149/1.1856988.
[32] Tang D, Lu J, Zhuang L, Liu P. Calculations of the exchange current density for hydrogen electrode reactions: a short review and a new equation. J Electroanal Chem 2010;644:144–9. https://doi.org/10.1016/j.jelechem.2009.11.031.
[33] Futamura S, Tachikawa Y, Matsuda J, Lyth SM, Shiratori Y, Taniguchi S, Sasaki K. SOFC anodes impregnated with noble metalcatalyst nanoparticles for high fuel utilization. Int J Hydrogen Energy 2019;44:8502–18. https://doi.org/10.1016/j.ijhydene.2019.01.223.
[34] Akkaya AV. Electrochemical model for performance analysis of a tubular SOFC. Int J Energy Res 2007;31:79–98. https://doi.org/10.1002/er.1238.
[35] Lee WY, Wee D, Ghoniem AF. An improved one-dimensional membrane-electrode assembly model to predict the performance of solid oxide fuel cell including the limiting current density. J Power Sources 2009;186:417–27. https://doi.org/10.1016/j.jpowsour.2008.10.009.
[36] Aguiar P, Adjiman CS, Brandon NP. Anode-supported intermediate temperature direct internal reforming solid oxide fuel cell. I: model-based steady-state performance. J Power Sources 2004;138:120–36. https://doi.org/10.1016/j.jpowsour.2004.06.040.
[37] Xie Y, Xue X. Modeling of solid oxide electrolysis cell for syngas generation with detailed surface chemistry. Solid State Ionics 2012;224:64–73. https://doi.org/10.1016/j.ssi.2012.07.015.
[38] Leonide A, Apel Y, Ivers-Tiffée E. SOFC modeling and parameter identification by means of impedance spectroscopy. ECS Trans 2009;19:81–109. https://doi.org/10.1149/1.3247567.
[39] García-Camprubí M, Izquierdo S, Fueyo N. Challenges in the electrochemical modelling of solid oxide fuel and electrolyser cells. Renew Sustain Energy Rev 2014;33:701–18. https://doi.org/10.1016/j.rser.2014.02.034.
[40] Williford RE, Chick LA, Maupin GD, Simner SP, Stevenson JW. Diffusion limitations in the porous anodes of SOFCs. J Electrochem Soc 2003;150:A1067–72. https://doi.org/10.1149/1.1586300.
[41] Chan SH, Khor KA, Xia ZT. A complete polarization model of a solid oxide fuel cell and its sensitivity to the change of cell component thickness. J Power Sources 2001;93:130–40. https://doi.org/10.1016/S0378-7753(00)00556-5.
[42] Jiang SP, Ramprakash Y. H2 oxidation on Ni/Y-TZP cermet electrodes-polarisation behaviour. Solid State Ionics 1999;116:145–56. https://doi.org/10.1016/S0167-2738(98)00269-0.
[43] Costamagna P, Honegger K. Modeling of solid oxide heat exchanger integrated stacks and simulation at high fuel utilization. J Electrochem Soc 1998;145:3995–4007. https://doi.org/10.1149/1.1838904.
[44] Mogensen M, Lindegaard T. The kinetics of hydrogen oxidation on a Ni-YSZ SOFC electrode at 1000°C. Proc Electrochem Soc 1993;1993–4:484–93. https://doi.org/10.1149/199304.0484PV.
[45] Armstrong EN, Duncan KL, Oh DJ, Weaver JF, Wachsman ED. Determination of surface exchange coefficients of LSM, LSCF, YSZ, GDC constituent materials in composite SOFC cathodes. J Electrochem Soc 2011;158:B492–9. https://doi.org/10.1149/1.3555122.
[46] Liu Z, Liu M, Yang L, Liu M. LSM-infiltrated LSCF cathodes for solid oxide fuel cells. J Energy Chem 2013;22:555–9. https://doi.org/10.1016/S2095-4956(13)60072-8.
[47] Sasaki K, Wurth JP, Gschwend R, Gödickemeier M, Gauckler LJ. Microstructure-property relations of solid oxide fuel cell cathodes and current collectors cathodic polarization and ohmic resistance. J Electrochem Soc 1996;143:530–43. https://doi.org/10.1149/1.1836476.
[48] Wang S, Kobayashi T, Dokiya M, Hashimoto T. Electrical and ionic conductivity of Gd-doped ceria. J Electrochem Soc 2000;147:3606–9. https://doi.org/10.1149/1.1393946.
[49] Mogensen M, Sammes NM, Tompsett GA. Physical, chemical and electrochemical properties of pure and doped ceria. Solid State Ionics 2000;129:63–94. https://doi.org/10.1016/S0167-2738(99)00318-5.

[50] Tuller HL. Mixed ionic-electronic conduction in a number of fluorite and pyrochlore compounds. Solid State Ionics 1992;52:135–46. https://doi.org/10.1016/0167-2738(92)90099-B.
[51] Blanksby SJ, Ellison GB. Bond dissociation energies of organic molecules. Acc Chem Res 2003;36:255–63. https://doi.org/10.1021/ar020230d.
[52] Nagata S, Momma A, Kato T, Kasuga Y. Numerical analysis of output characteristics of tubular SOFC with internal reformer. J Power Sources 2001;101:60–71. https://doi.org/10.1016/S0378-7753(01)00547-X.
[53] Udagawa J, Aguiar P, Brandon NP. Hydrogen production through steam electrolysis: model-based steady state performance of a cathode-supported intermediate temperature solid oxide electrolysis cell. J Power Sources 2007;166:127–36. https://doi.org/10.1016/j.jpowsour.2006.12.081.
[54] Papurello D, Iafrate C, Lanzini A, Santarelli M. Trace compounds impact on SOFC performance: experimental and modelling approach. Appl Energy 2017;208:637–54. https://doi.org/10.1016/j.apenergy.2017.09.090.
[55] Papurello D, Silvia S, Modena S. Biogas trace compounds impact on high-temperature fuel cells short stack performance. Int J Hydrogen Energy 2021;46:8792–801. https://doi.org/10.1016/j.ijhydene.2020.11.273.
[56] Lorent E, Millan M, Brandon NP. Use of gasification syngas in SOFC: impact of real tar on anode materials. Int J Hydrogen Energy 2012;37:7271–8. https://doi.org/10.1016/j.ijhydene.2011.11.047.
[57] Sasaki K, Haga K, Yoshizumi T, Minematsu D, Yuki E, Liu RR, et al. Chemical durability of solid oxide fuel cells: influence of impurities on long-term performance. J Power Sources 2011;196:9130–40. https://doi.org/10.1016/j.jpowsour.2010.09.122.